SI Text

Additional Plots of the Standard MJO Analog Wave. Figs. 2–4 showed only a few of the model variables; plots of other variables are included in SI Figs. 5–7. SI Fig. 6 includes plots of the moving average of vertical velocity, where w_j is the vertical velocity in the jth baroclinic mode. The shape and phase of w_1 strongly resemble that of P, and the shape and phase of w_2 strongly resemble that of $-H_s$. A comparison of w_1 and P is shown in SI Fig. 8. A constant was added to w_1 to make its minimum 0, and then w_1 was multiplied by a constant to make its maximum 1; the same was done to P to make its minimum 0 and maximum 1. After this rescaling, the two curves are indistinguishable, which means that P and w_1 are in phase and have the same shape. A similar comparison shows that H_s and $-w_2$ are also in phase and have the same shape. This relationship between vertical velocity and convective heating arises in other models from a weak temperature gradient (WTG) approximation (see ref. 1 and references therein). Thus the low frequency average of the propagating wave is balanced.

SI Fig. 9 shows a contour plot of the fluctuations of $P(x,t)$ about the wave-average (recall the wave average in SI Fig. 6). The fluctuations travel westward and are intense—often the fluctuations are stronger than the mean. SI Fig. 10 shows the standard deviation of the fluctuations about the wave-mean. The fluctuations are as strong as the mean for some variables. Also, although the fluctuations are mainly confined to the convectively active phase of the wave, there are also significant fluctuations in the convectively inactive phase of the wave. The role of these fluctuations in driving the wave will be analyzed below.

Transition to More Regular MJO Analog Waves. One might anticipate that the MJO analog weakens in strength as $\bar{\theta}_{eb} - \bar{\theta}_{em}$ is increased or $\tilde{Q}$ is decreased so that there is a transition to more regular—yet perhaps still chaotic—fluctuations in the MJO but with weaker small scale fluctuations. This occurs but the MJO analog waves remain remarkably like those depicted in the basic case until the transition value $\bar{\theta}_{eb} - \bar{\theta}_{em} = 15$ K, where there are only two linearly unstable wavenumbers (see Table 2). While it is difficult to supply a rigorous argument for the emergence of wavenumber-2 modes in Figs. 2–4, note from Table 2 that wavenumber-2 modes emerge from the stable regime as $\bar{\theta}_{eb} - \bar{\theta}_{em}$ decreases from 16 K to 15 K. This primary bifurcation branch with wavenumber 2 apparently continues to dominate at larger nonlinear amplitudes.

SI Figs. 11 and 12 depict the structure of the MJO analog wave for the case $\bar{\theta}_{eb} - \bar{\theta}_{em} = 15$ K. The wave moves at 7 m s^{-1} and SI Fig. 11 shows that both the deep convective events with much weaker amplitude and the westerly wind burst events remain chaotic within an extremely regular envelope that propagates on intraseasonal time scales. The time-averaged structure of the wave is presented in SI Fig. 12 together with the fluctuations in $P(x,t)$. Qualitatively, one sees a similar structure as in the standard case for the wave although it is more regular. While the standard deviation in the deep convection is only about 15–20% of the mean amplitude in the domain average, the standard deviation for the deep convection in the onset region centered around x =12,000 or 32,000 km is comparable to the mean value in the MJO analog wave. In the standard case, the strong turbulent fluctuations produced some asymmetry in the largely wavenumber-2 MJO analog while perfect wavenumber-2 symmetry is retained in the present case.

The Deep Convective Heating by the Mean State Versus the Mean of Fluctuating Heating. It is interesting to compare the structure and relative magnitude of the contribution of the deep convective heating of the low-frequency averaged propagating envelope by itself versus the mean of the fluctuating heating in driving the MJO analog wave as climatological parameters are varied. Let $\langle\cdot\rangle$ denote the time average in the travelling wave reference frame of any of the variables as depicted earlier in SI Figs. 6 and 12. The averaged contribution to the deep convective heating in the envelope is $\langle P\rangle$ in this notation with $P = \langle P\rangle + P'$. The relative contribution to the deep convective heating from the mean state alone is $P_{\langle\,\rangle}$ with

$$P_{\langle\,\rangle} = P(\langle\theta_{eb}\rangle, \langle q\rangle, \langle\theta_1\rangle, \langle\theta_2\rangle)$$

and the contribution from the fluctuations to the mean deep convective heating is $\langle P\rangle - P_{\langle\,\rangle}$. In SI Fig. 13, these quantities are graphed and compared as the climatological parameters vary through the four values $\bar{\theta}_{eb} - \bar{\theta}_{em} = 11$, 12, 14, and 15 K. The first thing that is apparent in SI Fig. 13 is the fact that the magnitude of the fluctuating contribution to the mean, $\langle P \rangle - P_{\langle\,\rangle}$, decreases in magnitude relative to $\langle P \rangle$ itself as $\bar{\theta}_{eb} - \bar{\theta}_{em}$ increases; this is anticipated by the linear stability results reported in Table 2 where the band of unstable waves shrinks with increasing $\bar{\theta}_{eb} - \bar{\theta}_{em}$ with reduced growth rate. However, note that in all four cases, the contributions from $\langle P \rangle - P_{\langle\,\rangle}$ in driving the large scale envelope are comparable in size or exceed $P_{\langle\,\rangle}$ itself in the onset/initiation region of the MJO analog wave; this is especially true for the three stronger cases with $\bar{\theta}_{eb} - \bar{\theta}_{em} = 11$, 12, and 14 K. Nevertheless, even in the weakest case with the most regular MJO analog wave with $\bar{\theta}_{eb} - \bar{\theta}_{em} = 15$ K, the same behavior for the contribution from the fluctuations to the mean envelope occurs with a very small magnitude. In all four cases, the largest peak for $\langle P \rangle - P_{\langle\,\rangle}$ occurs in the vicinity of the mean deep convection itself so that small scale fluctuations drive "flickering" in the deep convective structure in this wave. Similar results apply for variations in the climatological parameter $\tilde{Q}$ but are not shown here.

An Elementary Model for the Competition Between Propagating and Standing Modes. Given the system studied here with perfect symmetry between eastward and westward MJO analog waves without rotation, all the above numerical experiments document the emergence of travelling waves from symmetric initial data. This is far from obvious, since one might also speculate that such a system might have a propensity to produce standing waves which are a nonlinear superposition of the two opposite direction travelling waves with equal magnitude. Here we comment briefly on a simple ODE (ordinary differential equation) model developed earlier in a completely different physical context (2) that sheds light on the two possibilities. The results reported below are intended for qualitative interpretation in the present context rather than quantitative comparison.

Consider the situation as occurs with $\tilde{Q} = 1.0$ and $\bar{\theta}_{eb} - \bar{\theta}_{em} = 16$ K in Table 2 where this is only a single unstable wavenumber at $k = 2$. Let the real part of the complex formula

$$A_+(t)e^{i(kx+\omega t)}\mathbf{e}_+ + A_-(t)e^{i(kx-\omega t)}\mathbf{e}_- \qquad \textbf{[8]}$$

denote the amplitude of the wave where $A_\pm(t)$ denote the respective complex amplitudes of the eastward and westward waves, with $\mathbf{e}_\pm$ the corresponding eigenmodes from linear theory. Then weakly nonlinear perturbation analysis (2) yields the nonlinear system of two coupled ODEs for the amplitudes $R_\pm(t) = |A_\pm(t)|$,

$$\begin{aligned} \dot{R}_+ &= aR_+ - R_+^3 + bR_-^2 R_+ \\ \dot{R}_- &= aR_- - R_-^3 + bR_+^2 R_-, \end{aligned} \qquad \textbf{[9]}$$

where a and b are coefficients that depend on the nonlinear features of the physical system at hand. Note that Eq. **9** allows energy to be exchanged between the states $R_\pm$ for $b \neq 0$ and also the equations are identical if the roles of $R_\pm$ are interchanged. This is consistent with the behavior as in the present setting with perfect east/west symmetry. With Eqs. **8** and **9** it is easy to see the following for $b < 1$:

A) The east/west travelling waves have coordinates $(R_+, R_-) = (a^{1/2}, 0)$ or $(R_+, R_-) = (0, a^{1/2})$ and are steady solutions of Eq. **9**.

B) The nonlinear standing wave is a steady solution of Eq. **9** with equal coordinates $(R_+, R_-) = \left(\left(\frac{a}{1-b}\right)^{1/2}, \left(\frac{a}{1-b}\right)^{1/2}\right)$. **[10]**

Thus, we have a simple dynamical system in Eq. **9** representing travelling waves in Eq. **8** where, according to Eq. **10**, both nonlinear travelling waves and the standing wave coexist as solutions of the equation. Now consider general initial data R_+^0, R_-^0 and let's assess whether the general solution approaches one of the travelling waves in Eq. **10**A or the nonlinear standing wave in Eq. **10**B. Here is the answer from ref. 2: for $b < -1$, the general solution of Eq. **9** tends to one of the two travelling waves in Eq. **10**A, while for $-1 < b < 1$ the general solution always tends to the standing wave. Recall that the coefficient b reflects properties of the underlying physical system. Thus, by analogy with this much simpler physical system, the multicloud model in the present parameter regimes always prefer travelling waves rather than the standing wave in a fashion analogous to the behavior in the simple model with $b < -1$.

Self-Similarity and Linear Instability. What motivates the long time lags in Eq. **1** in the multicloud model? When the multicloud model was originally developed (3–6), it was used as a model for convectively coupled tropical waves on synoptic scales. The time scales used were roughly $\tau_s, \tau_c, \tau_{conv} \approx 2$ h, which were similar to time scales used in earlier models of convectively coupled waves (7–9). The central issue of this paper is to see whether it is possible to produce an MJO analog wave with realistic physical features by considering planetary scale behavior. Given the observed statistical self-similarity of tropical convection (10), it seems plausible that this could be achieved by using the multicloud model with τ_s, τ_c, and τ_{conv} given larger values to reflect the longer time scales of the MJO. This can be described mathematically in the following way, which is similar to the discussion in ref. 11.

First consider a system of conservation laws with source terms:

$$\frac{\partial}{\partial t}\mathbf{u} + \frac{\partial}{\partial x}\mathbf{f}(\mathbf{u}) = \mathbf{S}(\mathbf{u}), \tag{11}$$

where $\mathbf{u}$ is a vector with n components: $\mathbf{u} = (u_1, u_2, \cdots, u_n)^T$. Notice that the equations of the multicloud model in Eq. **5** take this form. When this system is linearized, it will have n plane wave solutions

$$\mathbf{v}_j(k) \exp\left(i[kx - \omega_j(k)t]\right), \qquad j = 1, 2, \cdots, n. \tag{12}$$

The oscillation frequency of each wave is Re $\omega_j(k)$, and the growth rate is Im $\omega_j(k)$. With values of $\tau_s, \tau_c, \tau_{conv} \approx 2$ hours, Khouider and Majda (3) obtained a wave with a finite band of unstable wavenumbers with the largest growth rate at a synoptic scale wavenumber called, say, k_*.

Now consider what happens when the source terms in Eq. **11** are modified by a factor of λ:

$$\frac{\partial}{\partial t}\mathbf{u} + \frac{\partial}{\partial x}\mathbf{f}(\mathbf{u}) = \lambda\mathbf{S}(\mathbf{u}). \tag{13}$$

When the system in Eq. **13** is linearized, it will have n plane wave solutions

$$\mathbf{v}_j\left(\frac{k}{\lambda}\right) \exp\left(i\left[kx - \lambda\omega_j\left(\frac{k}{\lambda}\right)t\right]\right), \qquad j = 1, 2, \cdots, n, \tag{14}$$

which reduces to the case in Eqs. **11–12** when $\lambda = 1$. If λ takes a value of $\lambda \approx 0.1$, which corresponds to longer time scales for the source terms, then notice what happens to the instability: the most unstable wavenumber is now λk_*, which will be on planetary scales if k_* is on synoptic scales. Furthermore, the frequency and growth rate of the wave now take the smaller values Re $\lambda\omega_j(k/\lambda)$ and Im $\lambda\omega_j(k/\lambda)$, which will be on intraseasonal time scales. Also notice that the source terms are smaller by a factor of $\lambda \approx 0.1$, and the physical structure of the most unstable wave, given by $\mathbf{v}_j(\lambda k_*/\lambda) = \mathbf{v}_j(k_*)$, has not changed. These features are all reflections of the statistical self-similarity of tropical convection.

While the above discussion is a clean illustration of linearly unstable waves that are self-similar, the real tropical atmosphere has some important deviations. For instance, in the discussion above, the waves have the same phase speed after the λ-rescaling: Re $\omega_j(k/\lambda)/(k/\lambda)$. Also, using a universal scale factor λ for all source terms would require rescaling the radiative cooling from 1 K day^{-1} to an unrealistic 0.1 K day^{-1}, and it would require rescaling all the time scales τ_s, τ_c, and τ_{conv} by the same factor. In the present paper, the radiative cooling takes the standard value of 1 K day^{-1}, and the time scales τ_s, τ_c, and τ_{conv} have not been rescaled from their values in ref. 3 by a universal scale factor λ. It is these deviations that lead to the important differences between the synoptic scale waves of refs. 3–6 and the planetary/intraseasonal scale waves of the present paper. At the same time, these deviations do not destroy the main point of the illustration in Eqs. **11**–**14**: from the perspective of linearly unstable waves, longer time lags for $\tau_s, \tau_c, \tau_{conv}$ are needed to obtain an unstable wave on planetary/intraseasonal scales with weaker convective heating.

Sensitivity Tests with τ_s, τ_c, and τ_{conv}. With the parameter choices for τ_s, τ_c, and τ_{conv} motivated by observations and by the mathematical illustration above, it is interesting to vary these three time scales within the intraseasonal regime. Recall that all the results previously discussed have utilized the fixed intraseasonal choice with $\tau_c = \tau_s = 7$ days and $\tau_{conv} = 12$ hours. SI Table 3 summarizes the results of linear stability analysis as these parameters are varied through a plausible intraseasonal range. The general trends are the following. First, as τ_c and τ_s are varied from 3 days to 11 days with τ_{conv} fixed, the amplitude of the growth rate remains roughly constant and at the planetary scales ($k = 3$), but the band of unstable waves increases as τ_s and τ_c increase; the phase of the unstable wave at wavenumber-3 decreases monotonically from 8 m s^{-1} for $\tau_s = \tau_c = 3$ days to 4.8 m s^{-1} for $\tau_s = \tau_c = 11$ days. When τ_{conv} is varied between 6 and 24 hours with τ_s, τ_c fixed to the standard value of 7 days, increasing τ_{conv} reduces the growth rate and the band of unstable wavenumbers while keeping the largest growth rates always on the planetary scales; also, the phase speed of the most unstable wave remains intraseasonal. The variation of the other parameters in the multicloud model in the present intraseasonal regime continues to follow all the trends documented previously for the multicloud model in the synoptic scale regime (3,6).

What Causes the Small-Scale Fluctuations? Another interesting question is: Which aspect of the multicloud model in Eq. **5** leads to the intermittent small scale fluctuations in the MJO analog wave in Figs. 2–4? As stated in Eq. **4**, the only nonlinearities in Eq. **5** occur through the convection switch Λ and the nonlinear moisture advection in Eq. **5**c. Consider momentarily the multicloud model with nonlinear moisture advection removed, in which case the q equation in Eq. **5** becomes

$$\frac{\partial q}{\partial t} + \frac{\partial}{\partial x}\left[\tilde{Q}u_1 + \tilde{\lambda}\tilde{Q}u_2\right] = -\frac{2\sqrt{2}}{\pi}P + \frac{1}{H_T}D.$$

With this modified q equation, all the linearized stability results reported earlier as guidelines do not change; this is because the equations are linearized about an RCE state with $\bar{q} = \bar{u}_1 = \bar{u}_2 = 0$, and quadratic nonlinear terms of the form $\partial_x(qu)$ do not affect linear theory with this trivial background state. The same numerical experiment of the standard case in Figs. 2–4 was repeated using the multicloud model with this modified q equation. An MJO analog wave emerged from the simulation, but most of the small scale fluctuations disappeared; in fact, under these circumstances, this more energetic parameter regime produced an MJO analog wave with a structure similar to the case shown in SI Figs. 11 and 12 (which was discussed above and used $\bar{\theta}_{eb} - \bar{\theta}_{em} = 15$ K, $\tilde{Q} = 1.0$, and included nonlinear moisture advection). Thus, nonlinear moisture advection is crucial in creating smaller scale fluctuations in deep convection.

Effect of Spatial Resolution. The effect of spatial resolution is interesting in the present model to understand how coarse resolution affects the behavior of the MJO analog wave. To test this, the numerical experiment of the standard case in Figs. 2–4 was repeated with the coarse resolution $\Delta x = 200$ km. First, the phase speed of the MJO analog wave increased slightly from 6.1 m s^{-1} to 6.6 m s^{-1}. However, as might be anticipated with such a complex multiscale wave, the fine scale fluctuations were lost and the structure of the wave which emerged strongly resembles the more regular fluctuating wave depicted earlier in SI Figs. 11 and 12.

Intraseasonal Variability with Nonuniform Sea Surface Temperature. Here we briefly discuss the resulting intraseasonal variability in the multicloud model with an imposed zonally varying value of θ^*_{eb}; the configuration is standard and involves one-half of a sine wave with strength ±5 K varying over 20,000 km with maximum strength at x =20,000 km and is described completely in Fig. 1 from ref. 4. In the results reported below, the parameters utilized in the multicloud model are those shown in Table 1 except $\tilde{\lambda} = 0.8$, $a_0 = 10$, $\tau_s = \tau_c = 6$ days, and $\bar{\theta}_{eb} - \bar{\theta}_{em} = 11$ K. The reason for this change is that the standard parameters utilized in Figs. 2–4 always yielded standing waves in the statistical steady state in the present configuration of variable sea surface temperature, although such results are not shown here; the goal here is to discuss scenarios with intraseasonal variability that prefer MJO analog travelling waves (as discussed above) rather than standing waves. The current choice of parameters achieves this.

The domain-averaged root mean square behavior of the model variables reported in SI Fig. 14a suggests that a statistical steady state has been achieved by the time $t = 1,000$ days. The deep convective heating is depicted on the time interval from $t = 1,200$ to 2,000 days in SI Fig. 14b. What is striking is the emergence of a train of MJO analog waves propagating through the warm pool from spontaneous locations and dying at the edge of the warm pool over the last 300 days in SI Fig. 14b. Surprisingly, a statistical steady state has not been achieved in the simulation despite the diagnostic in SI Fig. 14a. In fact, SI Fig. 15 depicts the behavior in the subsequent 250 days. The solution locks onto a propagating intraseasonal MJO analog wave with deep convection and a strong westerly wind burst that repeats itself with a regular period in time. This structure persists for 2,000 days beyond the results of SI Fig. 14.

In order to break the east/west symmetry, a uniform barotropic mean wind of -5 m s^{-1} was added to the two shallow water systems in the multicloud model in Eqs. **5**a and **5**b and the numerical experiment was carried out using the parameter values of Table 1 with the spatially varying θ^*_{eb}. Under these circumstances a statistical steady state was achieved in which the east/west symmetry is broken and eastward-travelling waves emerge; furthermore, the basic wave pattern has a slow modulation. The precipitation marking deep convection contours in this statistical steady state is reported in SI Fig. 16 while the velocity field at the bottom of the troposphere is reported in SI Fig. 17. The pattern that emerged has more intense westerly wind bursts in the MJO analog waves and strong deep convection in the time interval from $t = 1,300$ to 1,800 days and the absence of such effects for intervals of time both before and after this interval. While such a pattern repeats in the longer time series, it is truly chaotic in generating the more intense MJO analog propagating events.

References

1. Majda, A. J & Klein, R. (2003) *J. Atmos. Sci.* **60**, 393–408.
2. Bourlioux, A & Majda, A. J. (1995) *Phil. Trans. Roy. Soc. London A* **350**, 29–68.
3. Khouider, B & Majda, A. J. (2006) *J. Atmos. Sci.* **63**, 1308–1323.
4. Khouider, B & Majda, A. J. (2007) *J. Atmos. Sci.* **64**, 381–400.
5. Khouider, B & Majda, A. J. (2006) *Dyn. Atmos. Oceans* **42**, 59–80.
6. Khouider, B & Majda, A. J. (2006) *Theor. Comp. Fluid Dyn.* **20**, 351–375.
7. Betts, A. K & Miller, M. J. (1986) *Q. J. Roy. Met. Soc.* **112**, 693–709.
8. Mapes, B. E. (2000) *J. Atmos. Sci.* **57**, 1515–1535.
9. Majda, A. J & Shefter, M. G. (2001) *J. Atmos. Sci.* **58**, 1567–1584.
10. Mapes, B. E, Tulich, S, Lin, J.-L, & Zuidema, P. (2006) *Dyn. Atmos. Oceans* **42**, 3–29.
11. Majda, A. J. (2007) *J. Atmos. Sci.* **64**, 1393–1404.

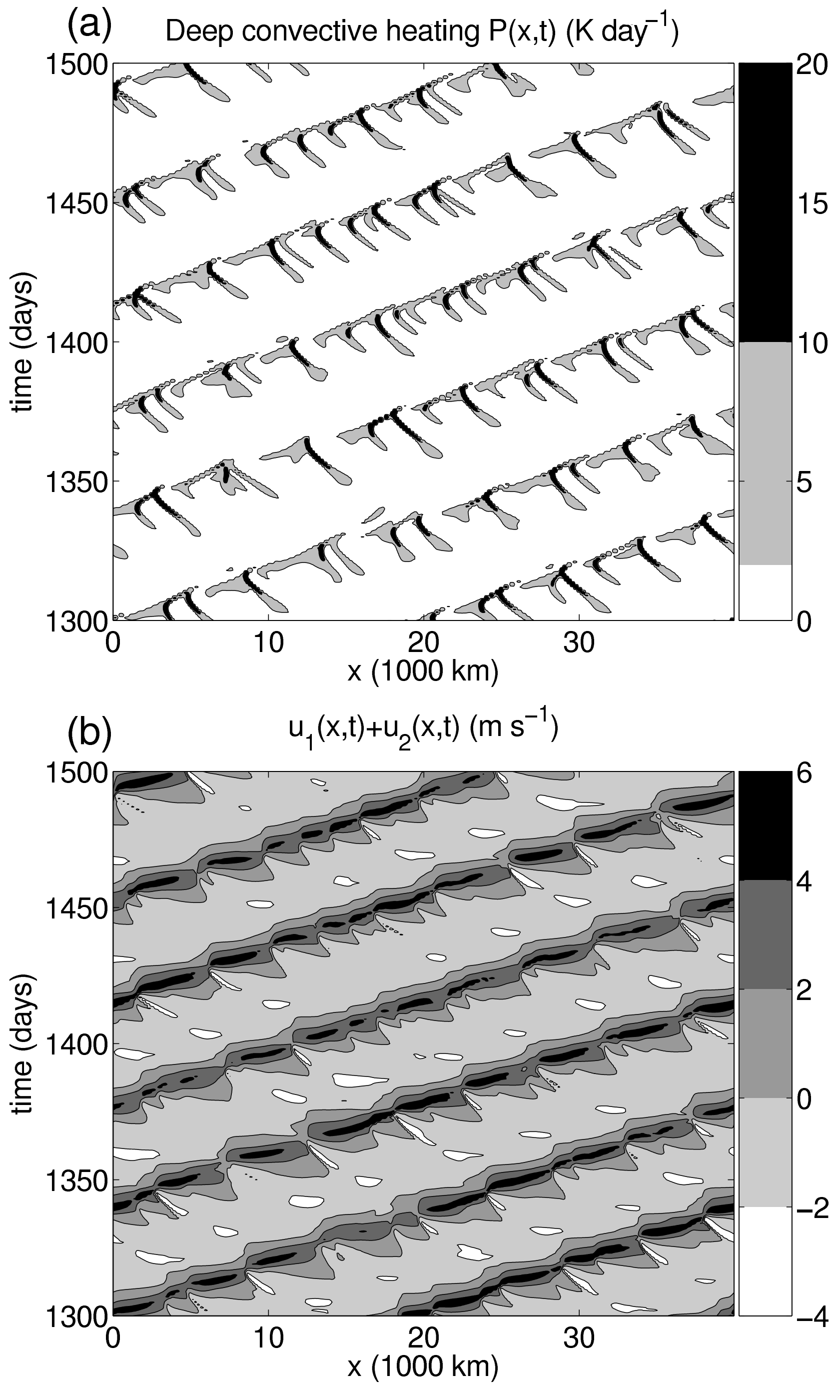

Figure 5: Numerical simulation of the multi-cloud model using the parameter values in Table 1. (Part of this figure is also shown in Fig. 2.) (a) Contour plot of the deep convective heating $P(x,t)$. Heating values above 2 K day^{-1} are shaded in gray and above 10 K day^{-1} in black. (b) Contour plot of the velocity at the bottom of the troposphere, $u_1(x,t) + u_2(x,t)$.

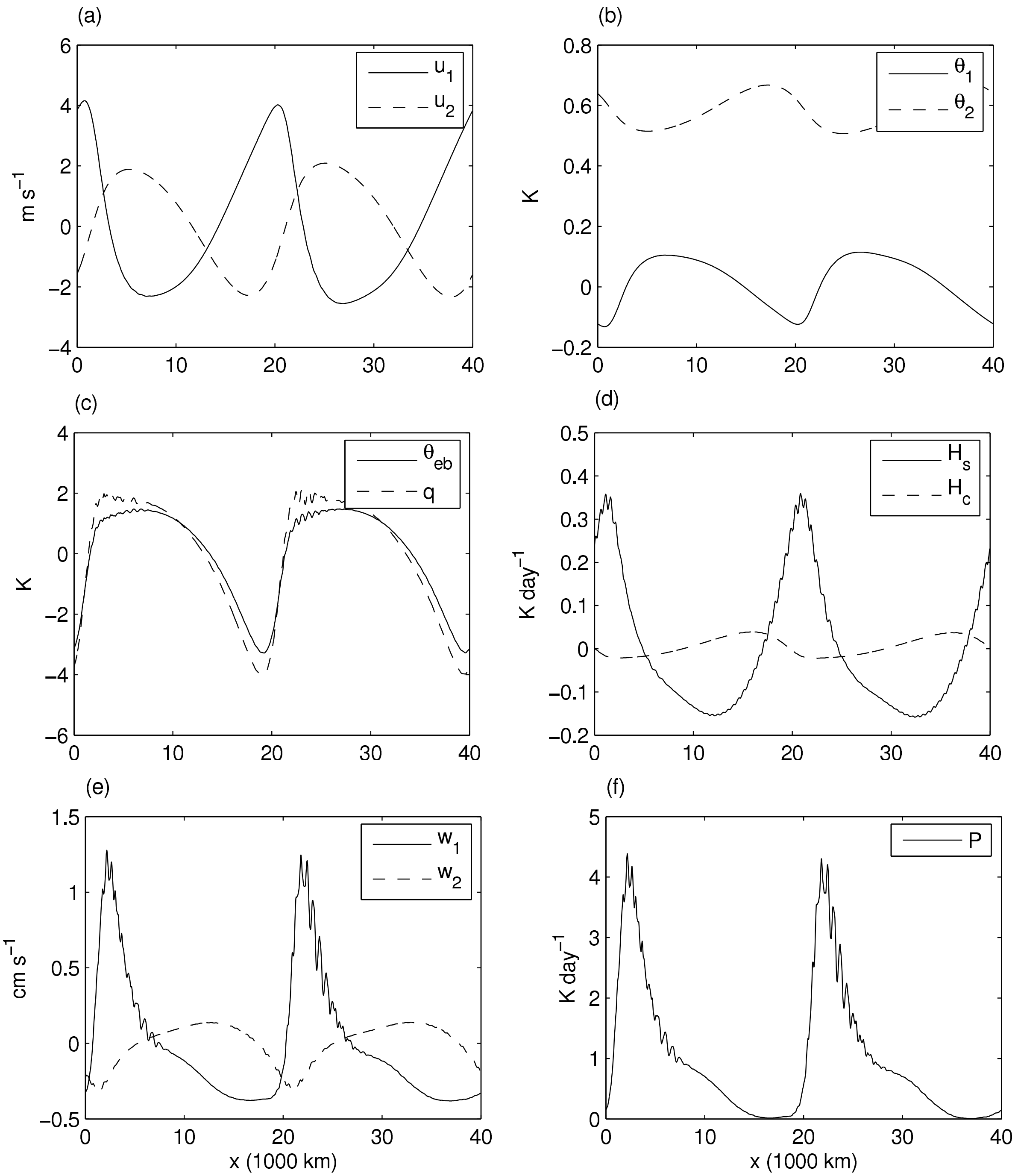

Figure 6: Moving average of model variables for the simulation in Fig. 5. (Part of this figure is also shown in Fig. 3.) The moving average was taken in a reference frame moving with the planetary-scale envelope of deep convection in Fig. 5, at 6 m s^{-1}. RCE values have been removed from all variables except P for these plots.

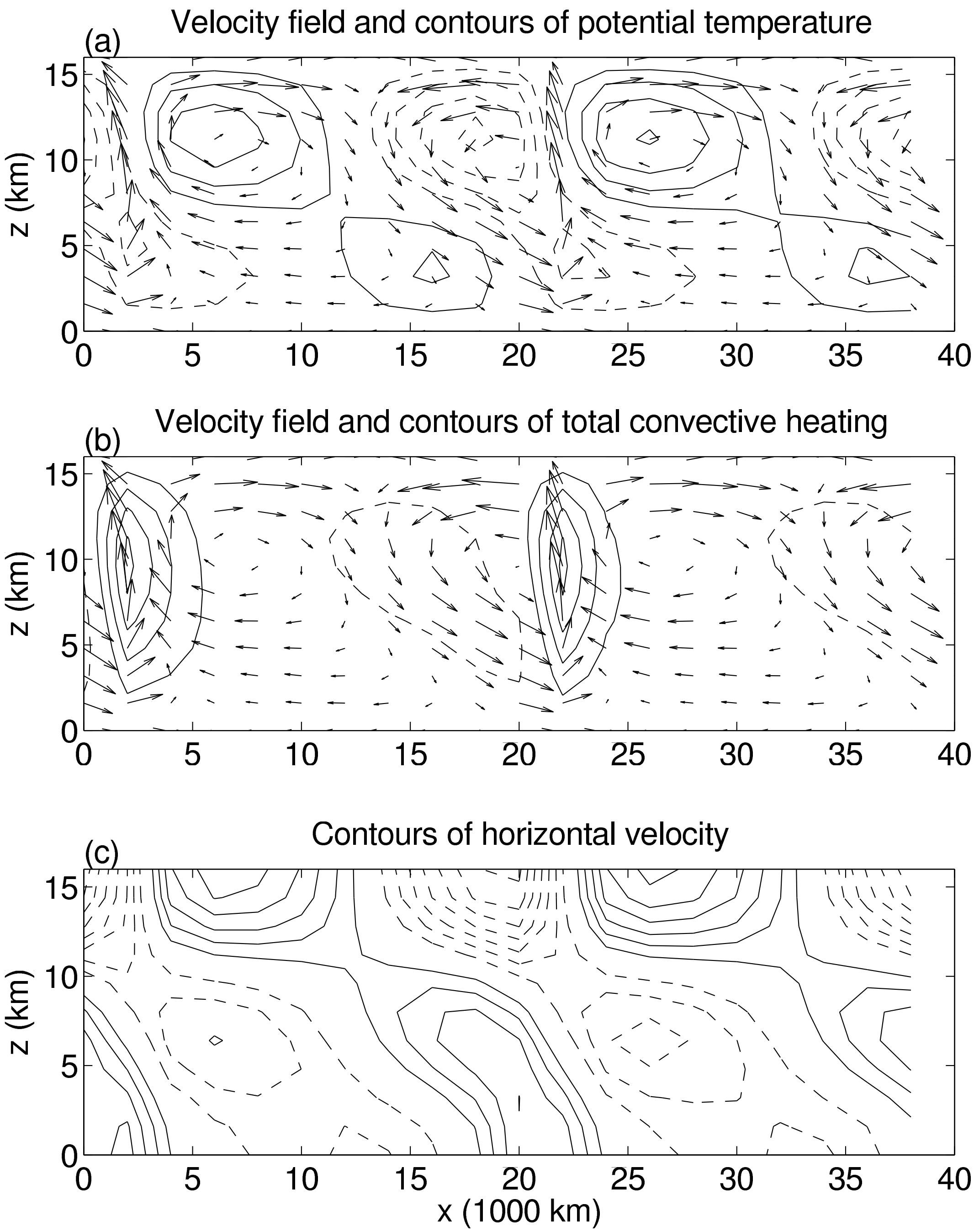

Figure 7: Moving average (as in Fig. 6) of model variables with their vertical structures. (Part of this figure is also shown in Fig. 4.) Dashed contours are for negative values, while solid contours are for positive values, with the zero contour removed. (a) Velocity field (U, W) with contours of potential temperature. The domain-means of θ_1 and θ_2 were removed for this plot (see Fig. 6b). Contour interval is 0.075 K. (b) Velocity field (U, W) with contours of total convective heating (congestus, stratiform, and deep convective heating combined). RCE values of P, H_s, H_c were removed for this plot. Contour interval is 1 K day^{-1}. (c) Contours of horizontal velocity with contour interval of 1 m s^{-1}.

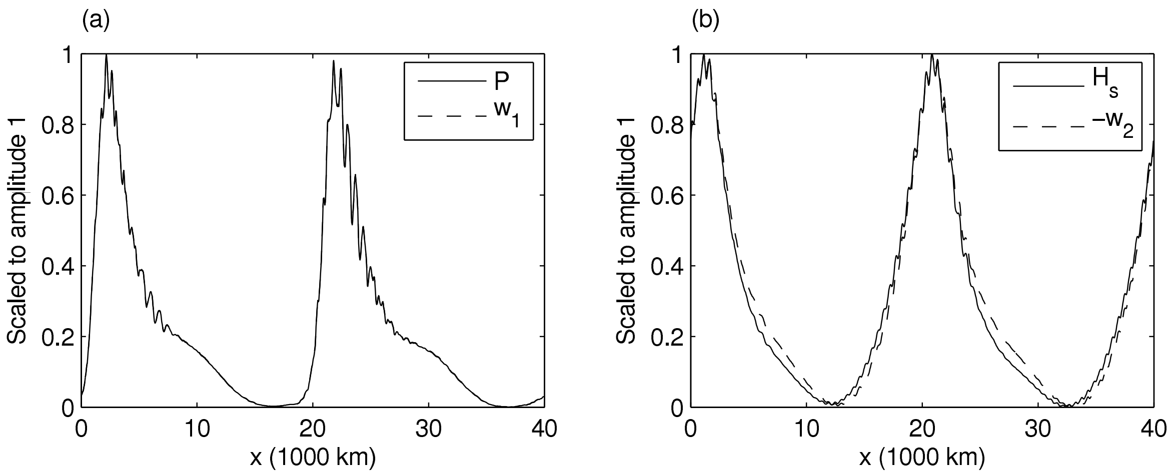

Figure 8: Scaled plots of moving averages of vertical velocity and convective heating from Fig. 6. The scaled vertical velocity and convective heating are balanced as in the weak temperature gradient (WTG) approximation.

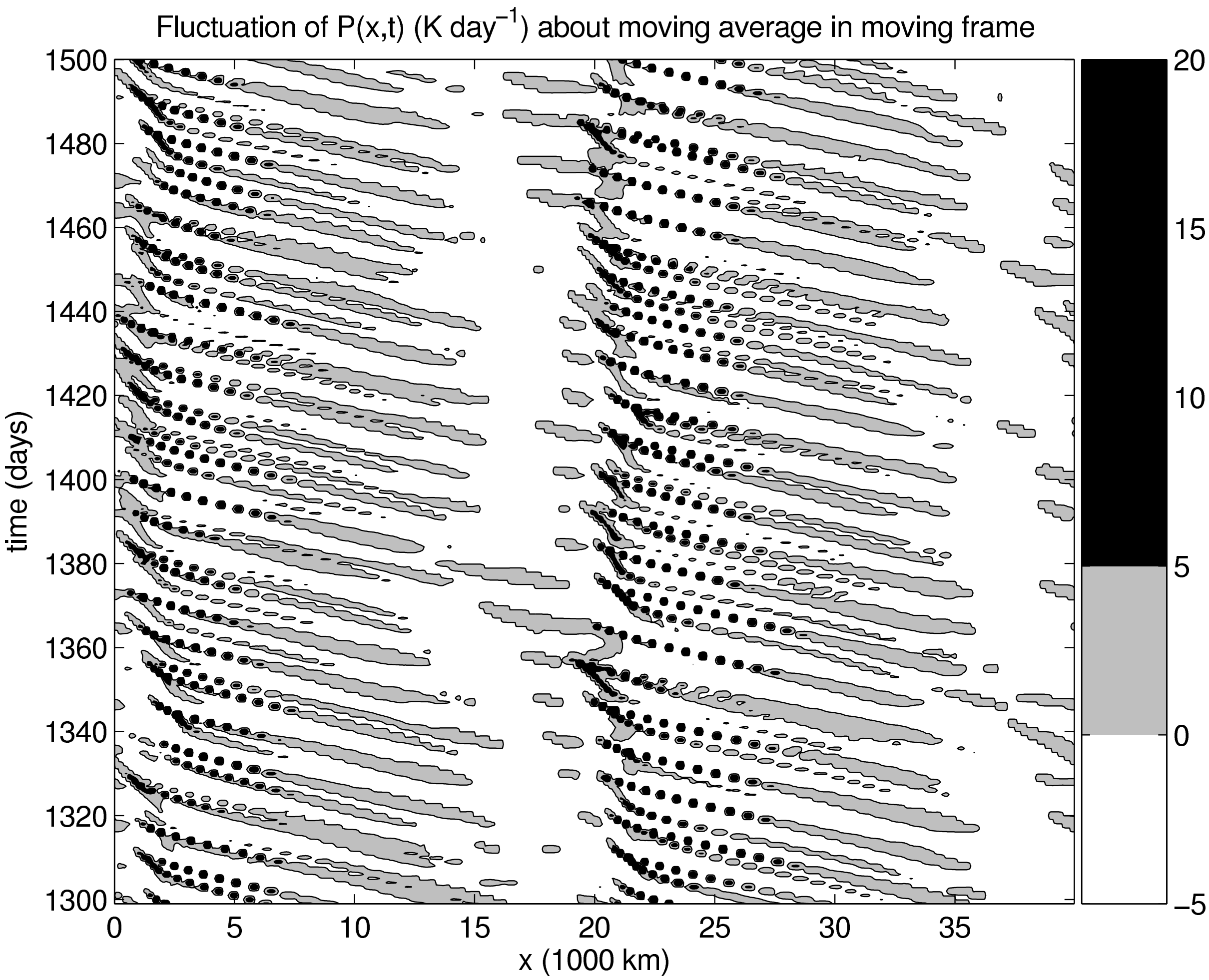

Figure 9: Fluctuation of deep convection $P(x,t)$ about its moving average. The fluctuations are shown here in the moving reference frame to emphasize the westward-propagating deep convection disturbances in the convectively active phase of the envelope. The moving average of $P(x,t)$ was shown in Fig. 6.

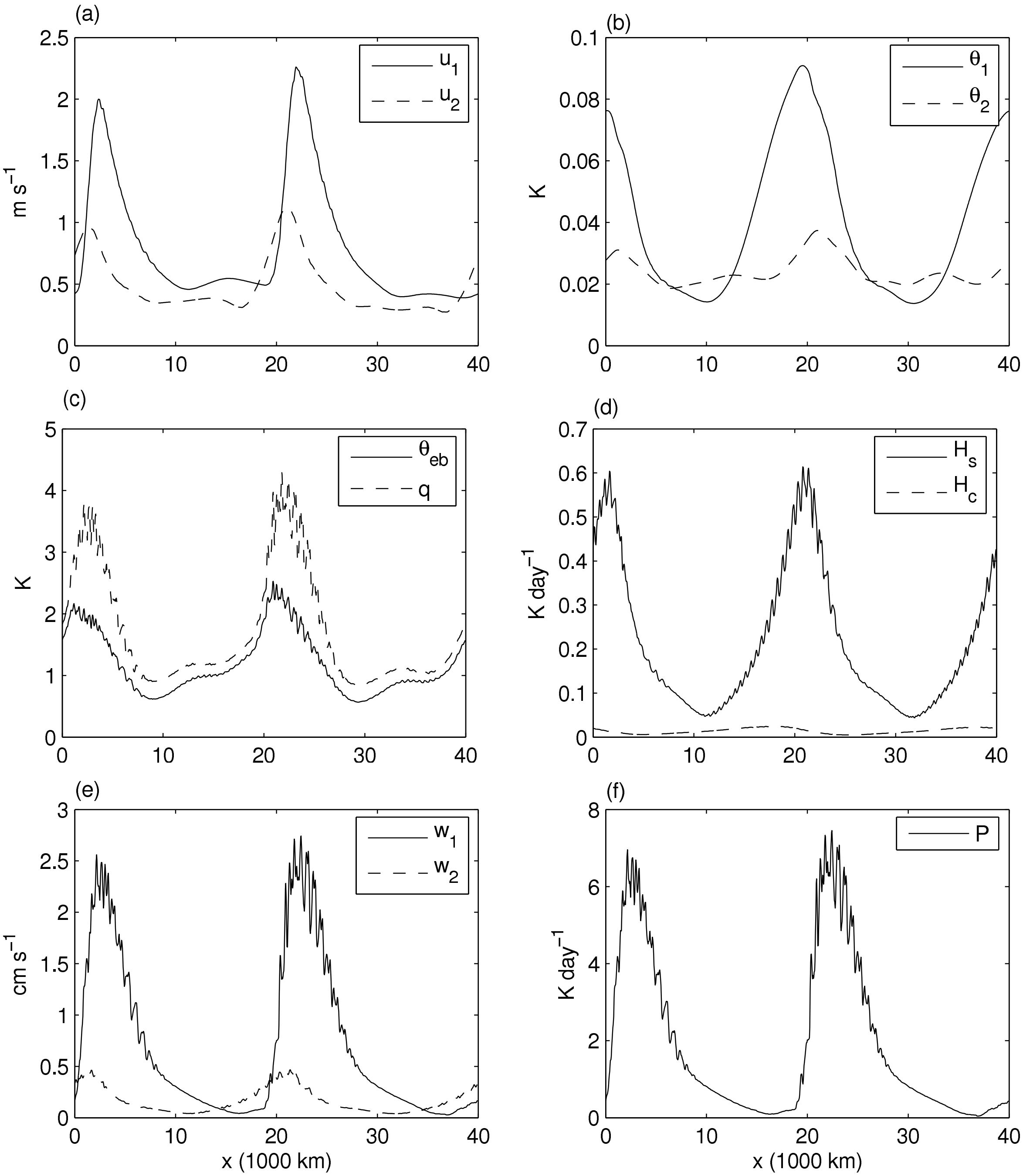

Figure 10: Standard deviations of the fluctuations about the moving averages from Fig. 6. While there are significant fluctuations in θ_{eb} and q in the inactive preconditioning phase, the strongest fluctuations are mainly confined to the convectively active phase of the wave, which is roughly $0 \leq x \leq$ 10,000 km and 20,000 km $\leq x \leq$ 30,000 km in the moving reference frame as shown here.

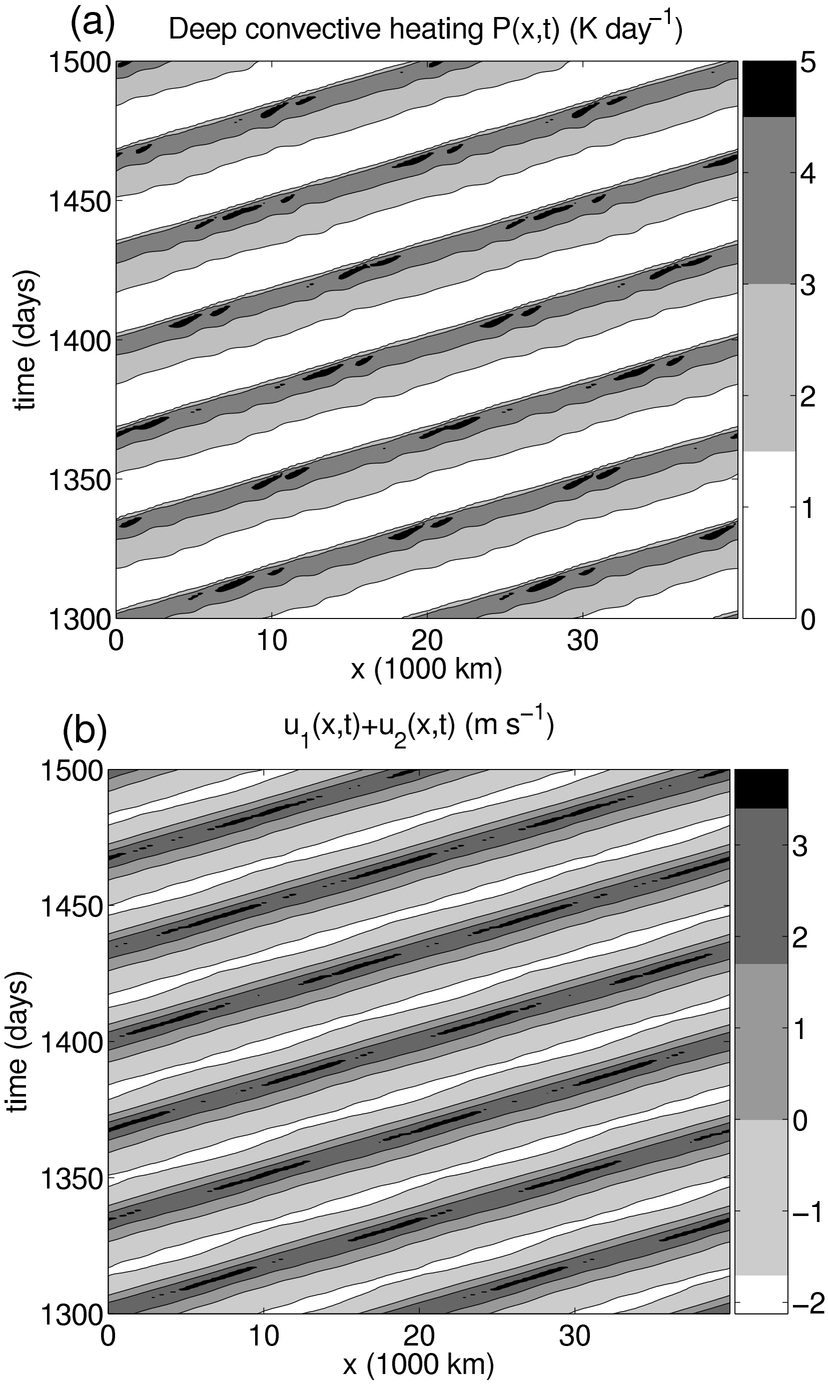

Figure 11: Numerical simulation of multi-cloud model using the parameter values from Table 1 except $\bar{\theta}_{eb} - \bar{\theta}_{em} = 15$ K. (a) Contour plot of the deep convective heating $P(x,t)$. (b) Contour plot of the velocity at the bottom of the troposphere.

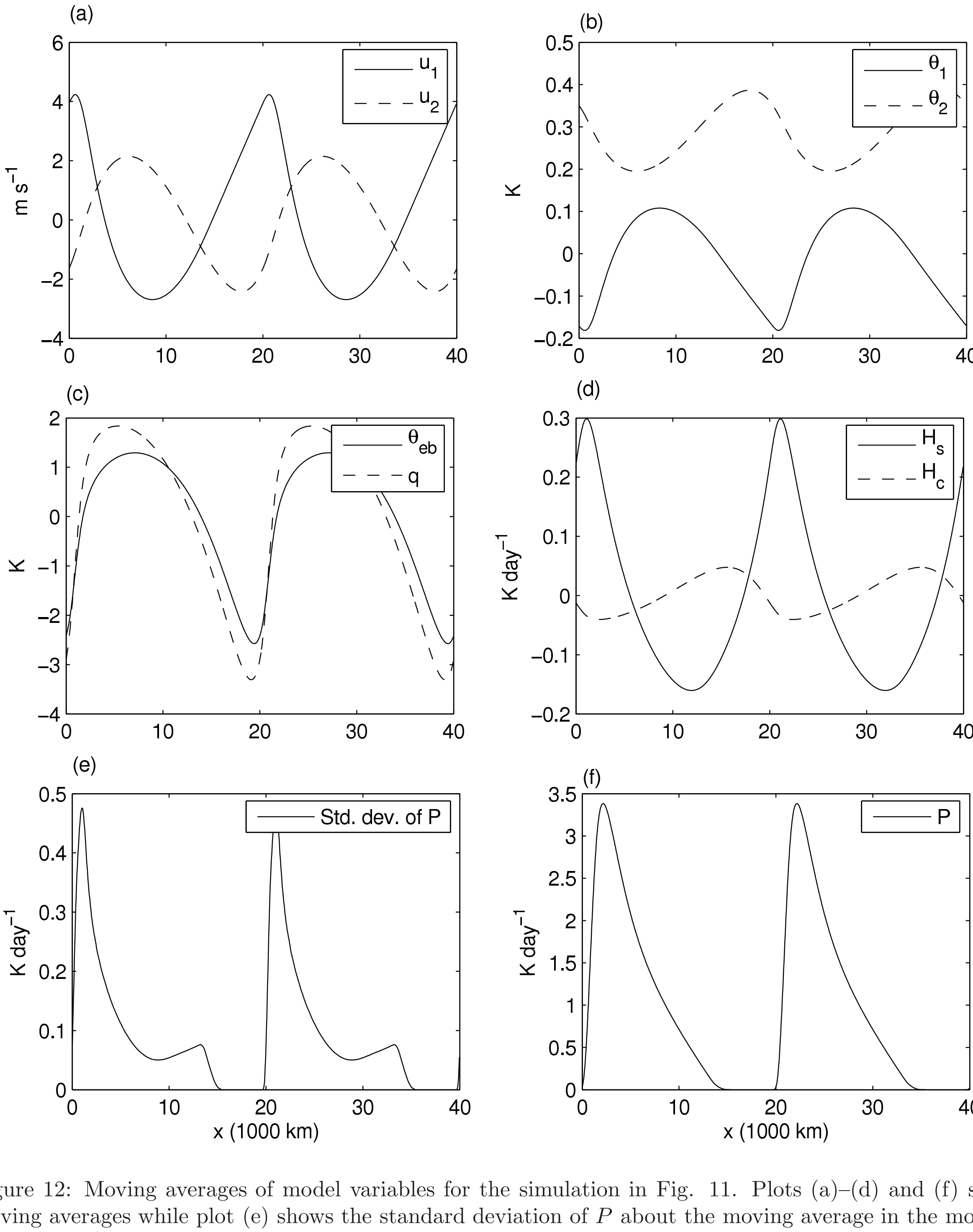

Figure 12: Moving averages of model variables for the simulation in Fig. 11. Plots (a)–(d) and (f) show moving averages while plot (e) shows the standard deviation of P about the moving average in the moving reference frame. The moving average was taken in a reference frame moving with the large-scale envelope of deep convection in Fig. 11, at 7 m s^{-1}.

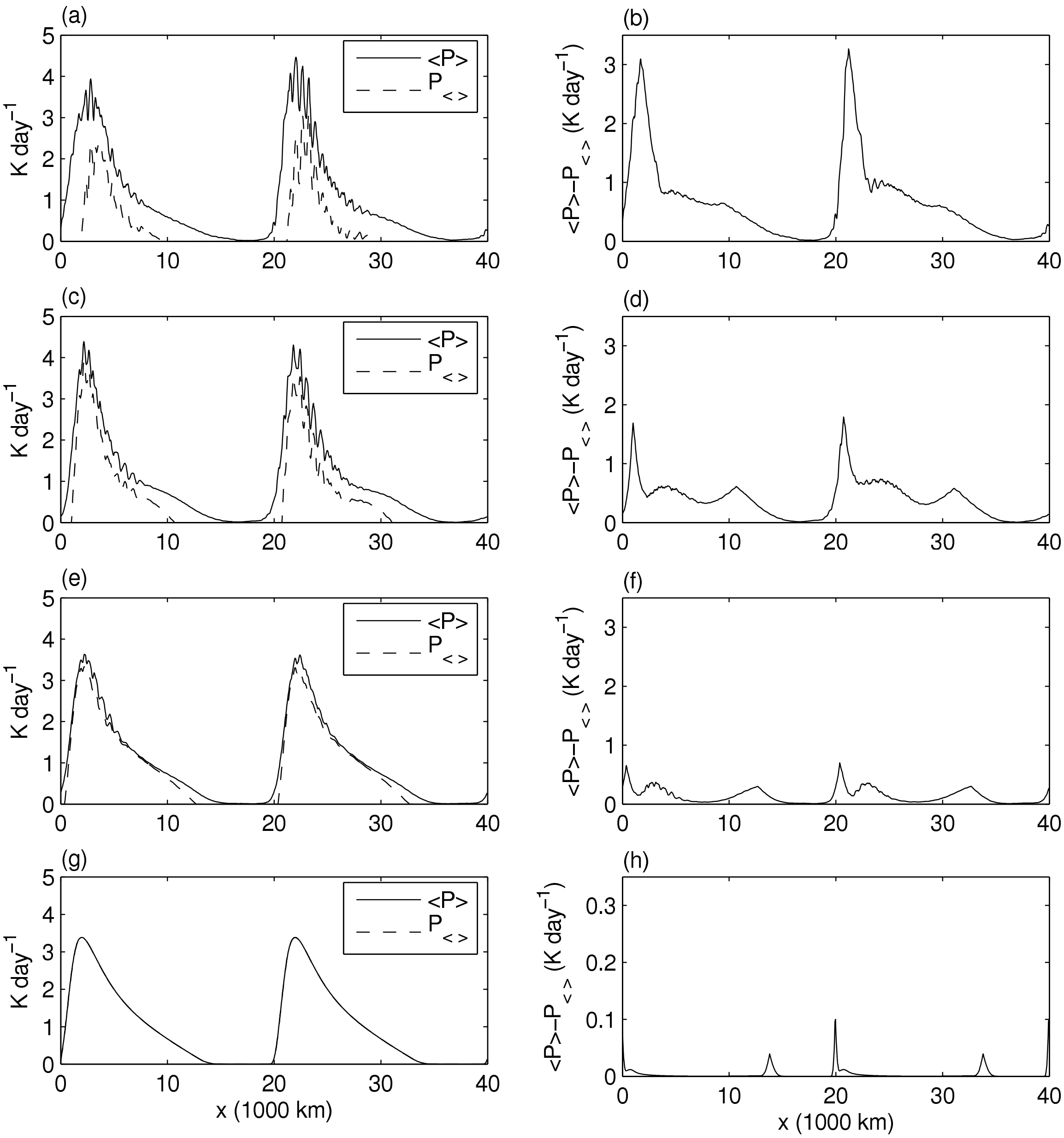

Figure 13: Moving average of deep convective heating $\langle P \rangle$ (left) and its two components: mean, $P_{\langle\rangle}$ (left), and fluctuation, $\langle P \rangle - P_{\langle\rangle}$ (right). Results are shown for four values of $\bar{\theta}_{eb} - \bar{\theta}_{em}$: 11 K [(a) and (b)], 12 K [(c) and (d)], 14 K [(e) and (f)], and 15 K [(g) and (h)]. All other parameters take the values shown in Table 1. Note that plot (h) uses a different axis limit than plots (b), (d), and (f). As $\bar{\theta}_{eb} - \bar{\theta}_{em}$ increases, the fluctuation $\langle P \rangle - P_{\langle\rangle}$ decreases.

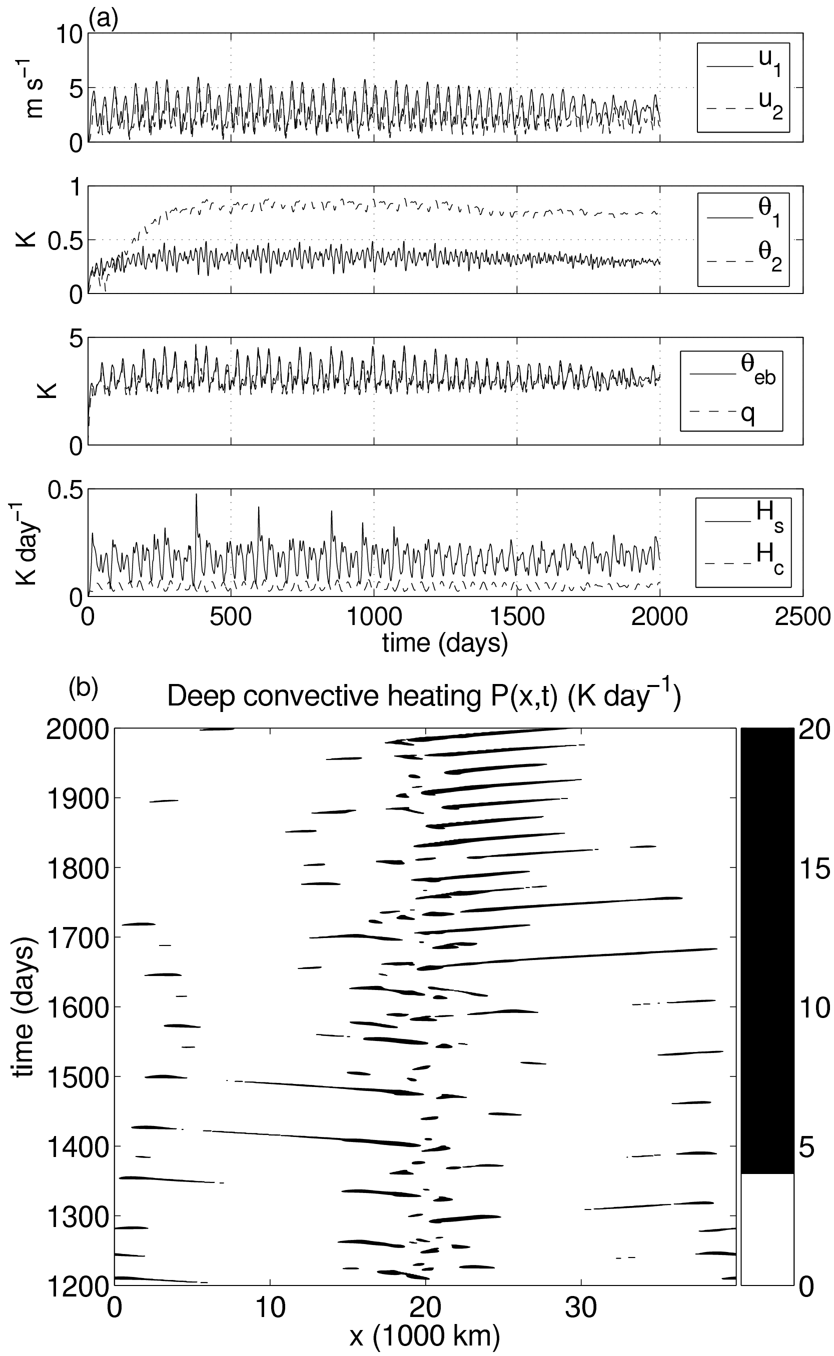

Figure 14: Numerical simulation of multi-cloud model using the parameter values from Table 1 except $\tilde{\lambda} = 0.8$, $a_0 = 10$, $\tau_s = \tau_c = 6$ days, and $\bar{\theta}_{eb} - \bar{\theta}_{em} = 11$ K. A warm pool SST profile is imposed through a spatially varying θ^*_{eb}, with a warm pool in the range 15,000 km$\leq x \leq$ 25,000 km. (a) Domain-averaged root mean square (RMS) of model variables. A statistical steady state appears to have been reached (but see the continuation in Fig. 15). (b) Contour plot of the deep convective heating $P(x,t)$.

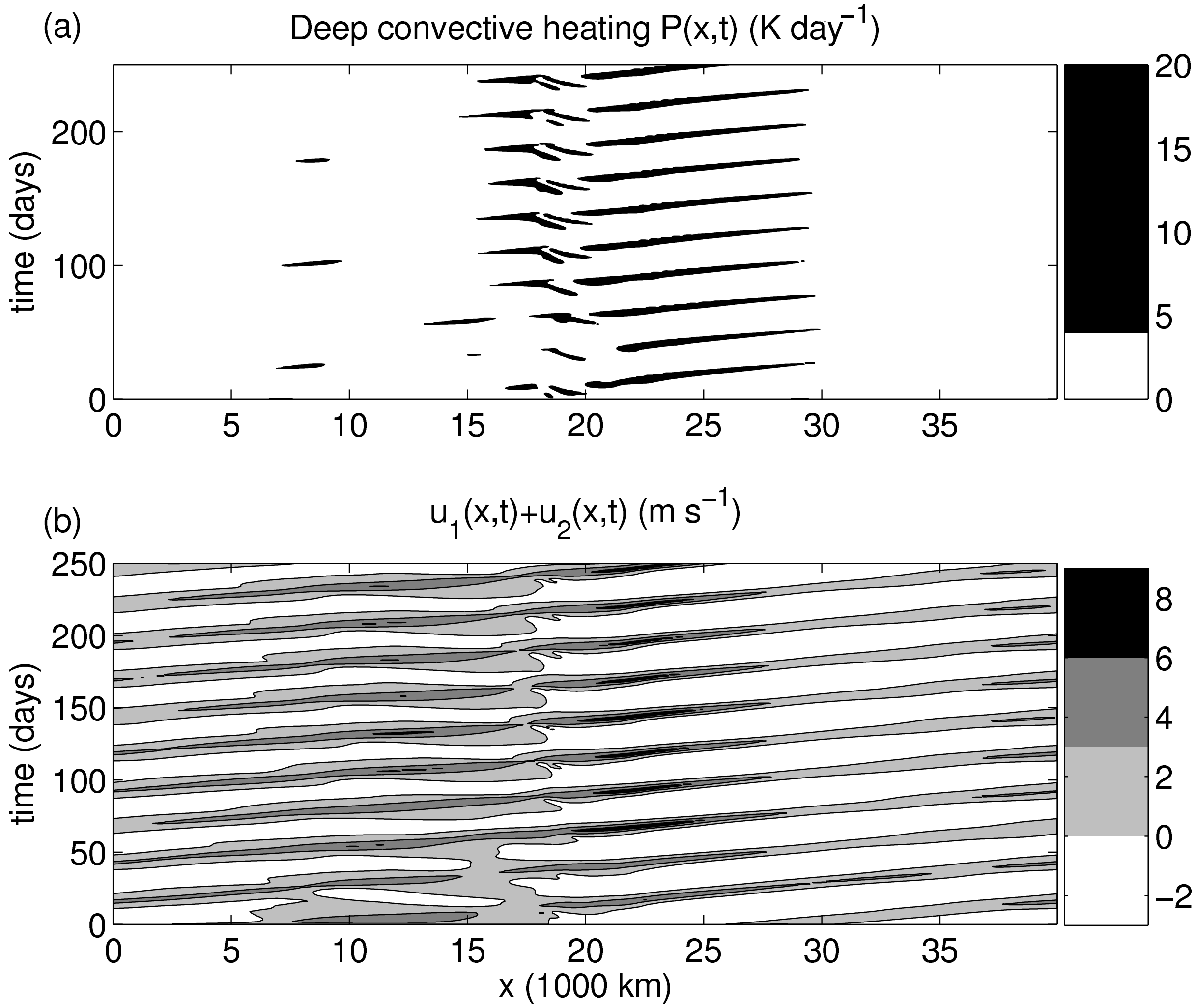

Figure 15: Continuation of Fig. 14, using the data from there at $t = 2000$ days as the initial condition. (a) Contour plot of the deep convective heating $P(x,t)$. (b) Contour plot of the velocity at the bottom of the troposphere, $u_1 + u_2$. The repeating pattern see from time $t = 100$ to 250 days persisted for as long as the simulation was run (for 1750 days beyond the data shown in this figure).

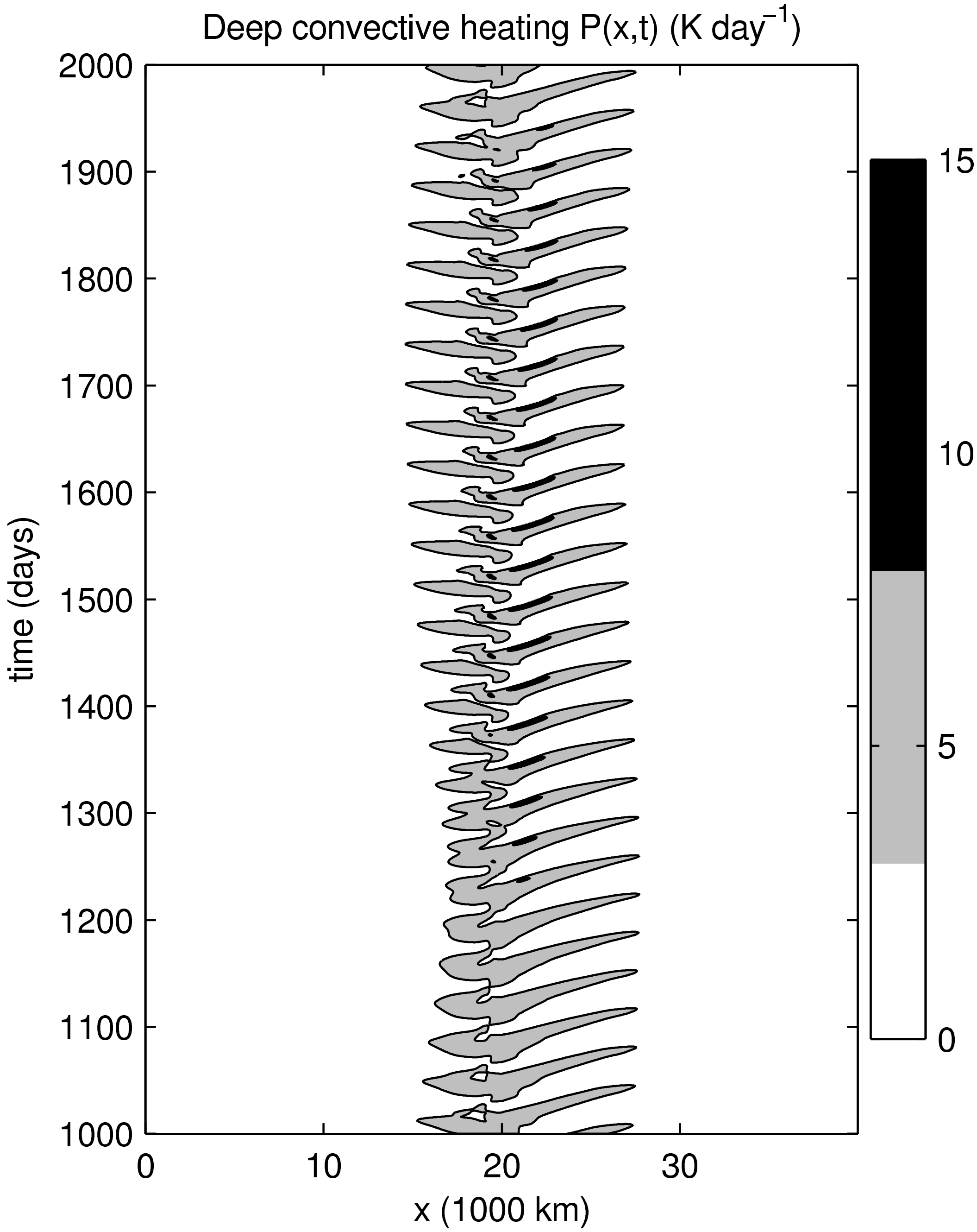

Figure 16: Numerical simulation of the multi-cloud model using the parameter values from Table 1; an easterly barotropic wind of -5 m $^{-1}$ was added to the shallow water systems in Eqs. **5a** and **5b**, and a non-uniform SST profile was imposed through a spatially varying θ^*_{eb} with a warm pool in the range 15,000 km$\leq x \leq$ 25,000 km. Shown here are contours of deep convective heating $P(x,t)$. Notice the slow modulation of P on a time scale of about 1000 days.

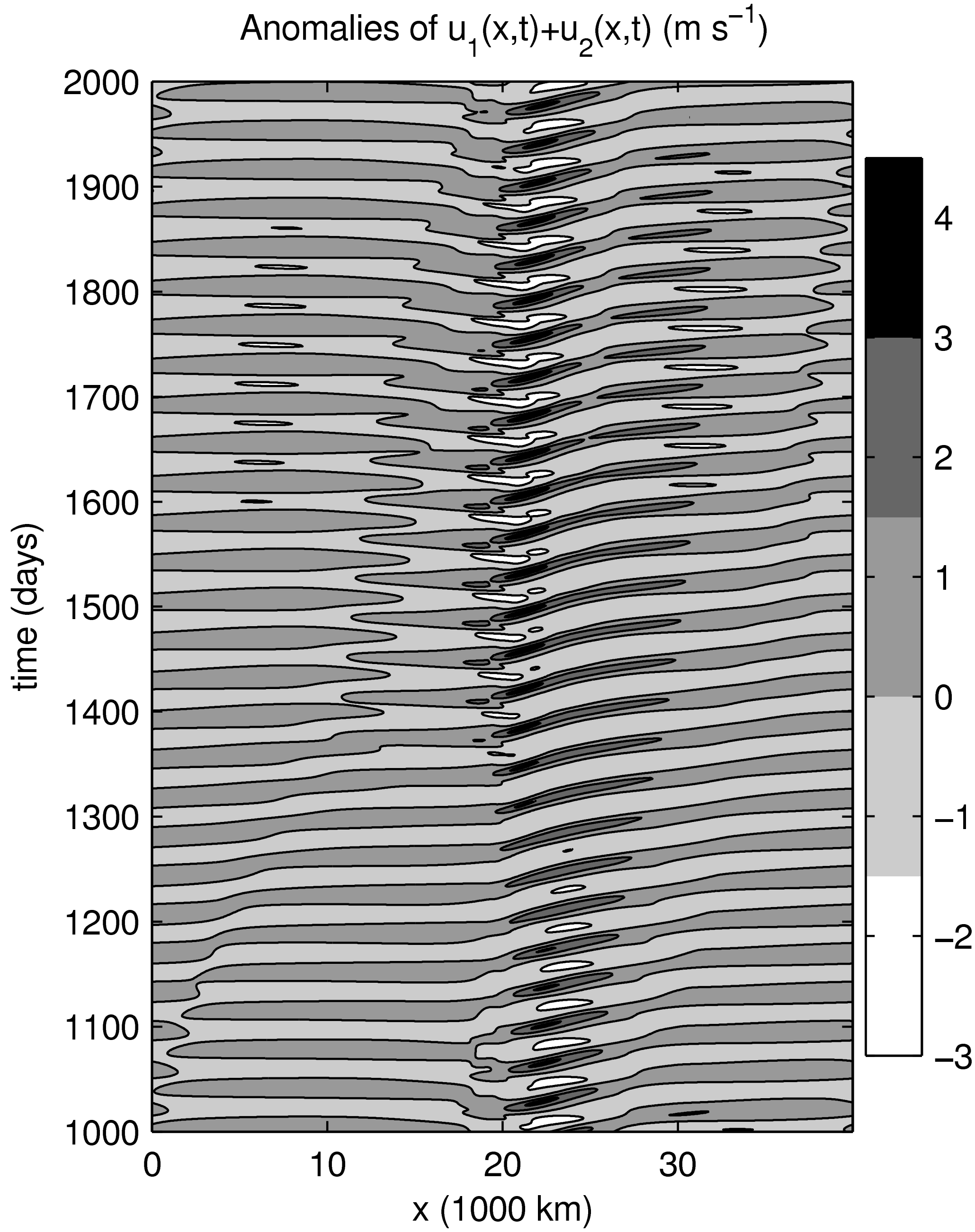

Figure 17: As in Fig. 16, but contours of $u_1 + u_2$, the velocity at the bottom of the troposphere, with the time-averaged Walker circulation removed.

Table 3: Behavior of the linearized MJO analog wave as τ_s, τ_c, and τ_{conv}—the stratiform, congestus, and deep convective time scales, respectively—are varied. The linear growth rate and phase speed at wavenumber k are denoted $\Gamma(k)$ and $c_p(k)$, respectively, and the wavenumber of the maximum growth rate is k_*. The wavenumber and phase speed of the simulated nonlinear wave are denoted k_{nl} and c_{nl}, respectively.

τ_{conv} (hours)	τ_s, τ_c (days)	k for which $\Gamma(k) > 0$	k_*	$\Gamma(k_*)$ (day^{-1})	$\lvert c_p(k_*)\rvert$ (m s^{-1})	$\Gamma(k=2)$ (day^{-1})	$\lvert c_p(k=2)\rvert$ (m s^{-1})	k_{nl}	$\lvert c_{nl}\rvert$ (m s^{-1})
12	3	2–5	3	0.021	8.0	0.009	9.3		
12	5	2–7	3	0.032	6.6	0.021	7.8	2	7.4
12	7	2–9	3	0.034	5.8	0.025	6.9	2	6.1
12	9	1–13	3	0.035	5.2	0.026	6.3	2	5.0
12	11	≥ 1	3	0.035	4.8	0.027	5.8		
6	7	≥ 1	7	0.096	3.8	0.040	6.7		
9	7	≥ 2	5	0.055	4.5	0.032	6.8		
12	7	2–9	3	0.034	5.8	0.025	6.9	2	6.1
18	7	2–3	2	0.011	7.0	0.011	7.0		
24	7	None							